JAMES | Journal of Advances in Modeling Earth Systems

RESEARCH ARTICLE
10.1029/2019MS001990

Three-Dimensional Radiative Effects By Shallow Cumulus Clouds on Dynamic Heterogeneities Over a Vegetated Surface

M. A. Veerman[1], X. Pedruzo-Bagazgoitia[1], F. Jakub[2], J. Vilà-Guerau de Arellano[1], and C. C. van Heerwaarden[1]

[1]Meteorology and Air Quality Group, Wageningen University and Research, Wageningen, Netherlands, [2]Meteorological Institute, Ludwig-Maximilians-Universität München, Munich, Germany

Key Points:

- We couple a 3-D radiative transfer solver to a LES with an interactive vegetated surface
- Displaced cloud shadows with 3-D radiative transfer result in thicker and larger clouds
- Heterogeneities in the surface heat fluxes are larger with 3-D than with 1-D radiative transfer

Correspondence to:
M. A. Veerman,
menno.veerman@wur.nl

Citation:
Veerman, M. A., Pedruzo-Bagazgoitia, X., Jakub, F., Vilà-Guerau de Arellano, J., & van Heerwaarden, C. C. (2020). Three-dimensional radiative effects by shallow cumulus clouds on dynamic heterogeneities over a vegetated surface. *Journal of Advances in Modeling Earth Systems*, *12*, e2019MS001990. https://doi.org/10.1029/2019MS001990

Received 13 DEC 2019
Accepted 21 MAY 2020
Accepted article online 28 MAY 2020

Abstract One-dimensional radiative transfer solvers are computationally much more efficient than full three-dimensional radiative transfer solvers but do not account for the horizontal propagation of radiation and thus produce unrealistic surface irradiance fields in models that resolve clouds. Here, we study the impact of using a 3-D radiative transfer solver on the direct and diffuse solar irradiance beneath clouds and the subsequent effect on the surface fluxes. We couple a relatively fast 3-D radiative transfer approximation (TenStream solver) to the Dutch Atmosphere Large-Eddy Simulation (DALES) model and perform simulations of a convective boundary layer over grassland with either 1-D or 3-D radiative transfer. Based on a single case study, simulations with 3-D radiative transfer develop larger and thicker clouds, which we attribute mainly to the displaced clouds shadows. With increasing cloud thickness, the surface fluxes decrease in cloud shadows with both radiation schemes but increase beneath clouds with 3-D radiative transfer. We find that with 3-D radiative transfer, the horizontal length scales dominating the spatial variability of the surface fluxes are over twice as large as with 1-D radiative transfer. The liquid water path and vertical wind velocity in the boundary layer are also dominated by larger length scales, suggesting that 3-D radiative transfer may lead to larger convective thermals. Our case study demonstrates that 3-D radiative effects can significantly impact dynamic heterogeneities induced by cloud shading. This may change our view on the coupling between boundary-layer clouds and the surface and should be further tested for generalizability in future studies.

Plain Language Summary Solar radiation warms the surface and provides energy for evaporation and biological processes, resulting in the release of heat and moisture to the atmosphere. This upward transport of warm and moist air eventually leads to the formation of clouds, which then alter the spatial distribution of solar radiation at the surface by partly reflecting and absorbing the incoming sunlight. Most previous studies that simulated these complex interactions between clouds, solar radiation, and the surface used 1-D radiation models. These are faster than 3-D radiation models but produce unrealistic surface solar radiation fields by only considering the vertical propagation of radiation. In this study, we use a relatively fast 3-D radiation model to simulate the formation of clouds and the surface heat and moisture fluxes. In our simulations, 3-D radiation results in thicker and wider clouds than 1-D radiation, predominantly because clouds no longer shade the surface beneath them when radiation propagates under an angle. Unlike in simulations with 1-D radiation, we find higher surface fluxes below clouds than under clear-sky and higher surface fluxes with increasing cloud thickness in simulations with 3-D radiation. Our results show that 3-D radiation may strongly impact the coupling between clouds and the land surface.

1. Introduction

Although the transfer of solar and thermal radiation is well understood (e.g., Liou, 2002), the extremely high computational costs of full 3-D radiative transfer solvers have necessitated trade-offs between accuracy and speed in atmospheric models. These include coarsening the temporal resolution of radiation calculations compared to the dynamical time step or solving radiative transfer in only one dimension, thus neglecting the horizontal transfer of energy. However, such 1-D radiative transfer solvers do not fully account for the complex horizontal interactions between radiation and other components of the system.

The interaction between clouds and radiation affects the atmosphere in two main ways. First, clouds intercept incoming solar radiation and both absorb and emit thermal radiation, leading to net radiative warming near the cloud base and net radiative cooling near the cloud top and cloud sides. This can enhance vertical motions in the cloud layer and may result in deeper and thicker clouds (Klinger et al., 2017). Second, clouds redistribute the incoming solar radiation, thereby modifying the spatial distribution of direct and diffuse radiative fluxes at surface. Lohou and Patton (2014) simulated the effect of cloud shading on surface heterogeneities and observed a decrease in sensible and latent heat flux and an increase in evaporative fraction of up to 30% in shaded areas. Horn et al. (2015) showed that dynamic heterogeneities due to cloud shading decrease boundary layer turbulence and result in smaller and shorter lived clouds. However, both studies used a 1-D radiative transfer scheme that only considered the vertical propagation of radiation. This leads to unrealistic surface irradiance fields because the displacement of clouds shadows with nonzero solar zenith angles is not accounted for. If cloud shadows are displaced sufficiently, the surface heat fluxes below clouds are not reduced by the shading and may continuously supply moisture and heat to the clouds. It is therefore important to investigate whether these 3-D effects can alter the horizontal length scales of clouds, dynamic heterogeneities at the surface, and convective thermals.

Schumann et al. (2002) was the first to investigate the effects of shifted cloud shadows due to a nonzero solar zenith angle on the atmospheric boundary layer (ABL) through large-eddy simulations but found no noticeable differences in turbulence or convection. Using the Tilted Independent Column Approximation (TICA), the application of 1-D radiative transfer to slanted columns (Várnai & Davies, 1999), Wapler (2007) observed that imposing a zero zenith angle reduces the life time of clouds but still has little effect on cloud cover, liquid water path (LWP), and boundary layer turbulence. Gronemeier et al. (2017) also used the TICA and found that the displacement of clouds shadows can generate secondary circulations and increase the lifetime of clouds if the solar zenith angle is sufficiently large. Jakub and Mayer (2017) used a more accurate 3-D radiative transfer solver (Jakub & Mayer, 2015) and a four-layer surface model and showed that the displacement of cloud shadows with 3-D radiation can be sufficient to trigger the formation of clouds streets, both with and without background wind, due to the dynamic heterogeneity caused by cloud shading at the surface. Such cloud shading-driven differences between 1-D and 3-D radiative transfer require a sufficiently fast response of the surface to changes in solar radiation and may therefore presumably only be observed over land.

The response of vegetation to changes in photosynthetically active radiation (PAR) is also an important factor in the coupling between clouds and the surface (Vilà-Guerau de Arellano et al., 2014; Pedruzo-Bagazgoitia et al., 2017; Sikma et al., 2018). Plants can adjust their stomatal aperture in response to changes in PAR to regulate the carbon uptake and transpiration of its leaves. Plants also respond differently to incoming direct or diffuse solar radiation, because the latter can come from any direction and is therefore distributed more homogeneously over the canopy (Kanniah et al., 2012; Li et al., 2014). The more homogeneous distribution of diffuse light increases the light use efficiency in the canopy (Kanniah et al., 2012). Pedruzo-Bagazgoitia et al. (2017) showed that, despite a decrease in total radiation, evaporation and photosynthesis are enhanced beneath optically thin clouds due to the higher diffuse radiation, although this enhancement can only be observed in simulations without background wind (Sikma et al., 2018).

Since Pedruzo-Bagazgoitia et al. (2017) and Sikma et al. (2018) both solved radiative transfer in 1-D, cloud shadows were located directly below the clouds. With 3-D radiative transfer, the effect of clouds on the local partitioning between direct and diffuse radiation is likely different due to horizontal scattering and displaced cloud shadows. Therefore, it is interesting whether the enhanced photosynthesis due to thin clouds found by Pedruzo-Bagazgoitia et al. (2017) can still be observed with 3-D radiation and sufficiently large zenith angles when clouds are not shading the surface beneath them.

In this study, we perform a case study to investigate how accounting for the three-dimensional propagation of radiation with nonzero solar zenith angles affects the dynamic heterogeneities induced by cloud shading and the thermal structure of the boundary layer over a vegetated surface. To this end, we use large-eddy simulations of a convective boundary layer, in which shallow cumulus clouds develop in the early afternoon (Vilà-Guerau de Arellano 2014; Pedruzo-Bagazgoitia et al., 2017). Our interests are in the cloud-induced partitioning between direct and diffuse radiation with 3-D radiation and the subsequent effects on the local surface fluxes. Furthermore, we aim to find whether 3-D radiative effects can alter the dominant horizontal length scales of the surface heat fluxes, boundary layer turbulence, and clouds.

Table 1
Overview of the Six Experiments

Name	Radiation	Explanation
`2-stream`	RRTMG	Main experiment with RRTMG
`10-stream`	TenStream	Main experiment with the TenStream solver
`2-stream_smooth`	RRTMG	RRTMG with domain-averaged diffuse radiation at the surface
`10-stream_smooth`	TenStream	TenStream solver with domain-averaged diffuse radiation at the surface
`Transparent`	RRTMG	RRTMG with transparent clouds (τ=0 in the radiation scheme)

The structure of the remainder of this paper is as follows. The radiative transfer models, the interactive surface scheme, and our numerical experiments are described in section 2. Section 3 gives a short overview of the additional computational costs of the 3-D radiative transfer solver used in our experiments. In section 4, we present and discuss the results: Section 4.1 describes the development of the general cloud and boundary layer characteristics and the domain-averaged surface fluxes. Section 4.2 describes the effects of clouds on the local surface heat fluxes and on the characteristic length scales in the atmosphere and at the surface. The main conclusions of this study are provided in section 5.

2. Methodology

We perform five experiments (Table 1) using the Dutch Atmospheric Large-Eddy simulation (DALES) (Heus et al., 2010; Ouwersloot et al., 2017), Version 4.1, with an interactive land surface (van Heerwaarden et al., 2010). The simulations are done with either a 1-D or a 3-D radiative transfer solver. The Rapid Radiative Transfer Model for use in General Circulation Models (RRTMG) (Iacono et al., 2008; Mlawer et al., 1997) is used for 1-D radiative transfer, and the TenStream solver (Jakub & Mayer, 2015) is used as the 3-D radiative transfer solver. Figure 1 is a snapshot of the two main experiments with RRTMG and with the TenStream solver (section 2.3), which shows the coupling between clouds and the interactive land surface with 1-D and with 3-D radiative transfer.

2.1. Radiative Transfer Models

RRTMG (Iacono et al., 2008) is a modification of the Rapid Radiative Transfer Model (Clough et al., 2005; Mlawer et al., 1997), a broadband radiation model with high accuracy benchmarked to the line-by-line radiative transfer model (LBLRTM; Clough et al., 1992). RRTMG uses 16 longwave (10 – 3,250 cm^{-1}) and 14 shortwave (820 – 50,000 cm^{-1}) spectral bands and spectrally integrates within each band using the correlated k-distribution method (Fu & Liou, 1992), using between 2 and 16 *g*-points per spectral band (Mlawer et al., 1997). RRTMG first calculates all optical properties at each *g*-point and then uses a two-stream radiative transfer solver (Oreopoulos & Barker, 1999) to calculate the radiative fluxes.

The TenStream solver (Jakub & Mayer, 2015) is a relatively computationally efficient 3-D radiative transfer solver. It produces significantly more accurate heating rates, with respect to highly accurate Monte Carlo methods than 1-D radiative transfer solvers (Jakub & Mayer, 2015) by accounting for the horizontal propagation of radiation. RRTMG is used to calculate optical properties, and spectral integration is performed with a correlated k-distribution method. The solver uses adaptive spectral integration; that is, at most of the radiation time steps, only the spectral bands that have changed significantly are recomputed. The TenStream solver uses three streams for direct shortwave radiation and 10 streams for diffuse shortwave radiation: for direct radiation one downward stream and one stream each in east-west and south-north direction, for diffuse radiation an upward and downward stream at the top and bottom of each gridbox, and additional diagonally upward and diagonally downward streams at each vertical face (Jakub & Mayer, 2015). For longwave radiation, the TenStream solver only uses the 10 diffuse streams. While the TenStream solver may be over 2 orders of magnitude faster than full 3-D radiative transfer solvers (e.g., Monte Carlo) when clouds are present, its computational costs can still be about 2 orders of magnitude larger than those of 1-D radiative transfer solvers (section 3).

Based on a set of seven clouds fields, Figures 2a–2d show the partitioning of direct and diffuse solar radiation by the Monte Carlo code for the physically correct tracing of photons in cloudy atmospheres (MYSTIC; Emde et al., 2016; Mayer, 2009), the TenStream solver, the TenStream solver with horizontally averaged diffuse radiation at the surface, and a δ-Eddington two-stream solver, respectively. Because radiation only propagates vertically with 1-D radiative transfer, the response of the incoming radiation at the surface to the enhanced scattering and absorption of radiation by clouds is quite straightforward: Beneath optically thin clouds (cloud optical depth <8 Min; 2005), the surface receives increasingly less direct but more diffuse shortwave radiation as clouds get thicker (Figure 2d, from lower-right to upper-left corner), whereas beneath optically thicker clouds (Figure 2d, from upper-left to bottom-left corner) the direct and diffuse radiation

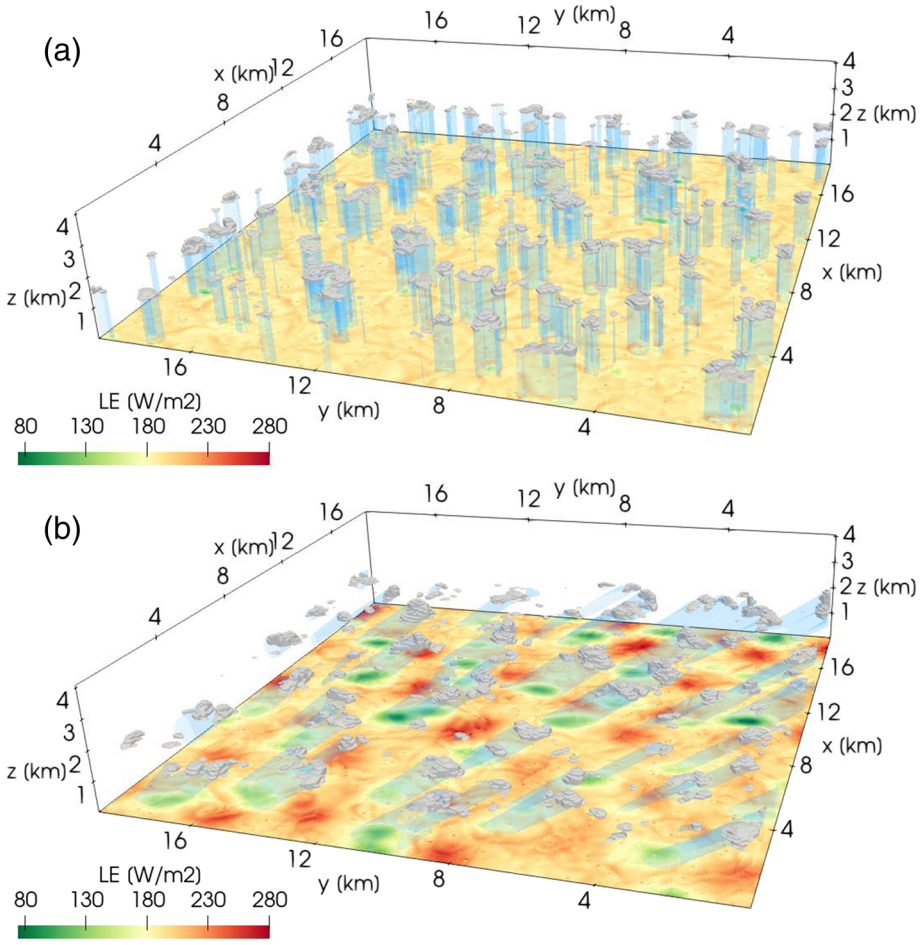

Figure 1. Cloud field at 12:32 UTC of the main `2-stream` (a) and `10-stream` (b) experiments (see section 2.3) and the surface latent heat flux. Gray colors indicate clouds, that is, all grid cells containing liquid water. Blue shades indicate all grid cells where the direct downwelling shortwave flux is less than 450 W m^{-2} (cloud shadows).

both decrease as clouds thicken (Pedruzo-Bagazgoitia et al., 2017). With MYSTIC (Figure 2a), our benchmark for 3-D radiative transfer, the diffuse radiation is distributed quite homogeneously over the surface, between 125 and 200 W m^{-2} regardless of the amount of direct radiation. The reason for this is that the incoming radiation at the surface does not depend only on the presence and thickness of clouds in the column above: Cloud shadows, denoting a decrease in direct radiation, are displaced (depending on the solar zenith angle), and diffuse radiation is also scattered from neighboring cloudy columns. With the TenStream solver, however, the relation between direct and diffuse radiation is quite nonlinear (Figure 2b). The patches in the TenStream simulation with less or more diffuse radiation than found in MYSTIC indicate that the TenStream is insufficiently diffusive (Jakub & Mayer, 2015), resulting in areas near or below clouds receiving too much and areas under clear sky receiving too little diffuse radiation. Nevertheless, the surface shortwave irradiance is clearly better represented with the TenStream solver than with 1-D radiation (Figure 2e). If we horizontally average all diffuse radiation at the surface (Figure 2c), we clearly underestimate the diffusivity of radiation compared to MYSTIC, that is, all diffuse radiation enhancements near clouds are smoothened out.

2.2. Surface Scheme

The interactive land surface representations consist of a four-layer model that solves the evolution of soil temperature and soil moisture. The upper soil layer interacts with the atmosphere via a model that solves the energy budget of vegetated surfaces (Heus et al., 2010). The photosynthesis rate and the canopy resistance are calculated with the plant-physiology-based A-gs model that has been successfully tested on low

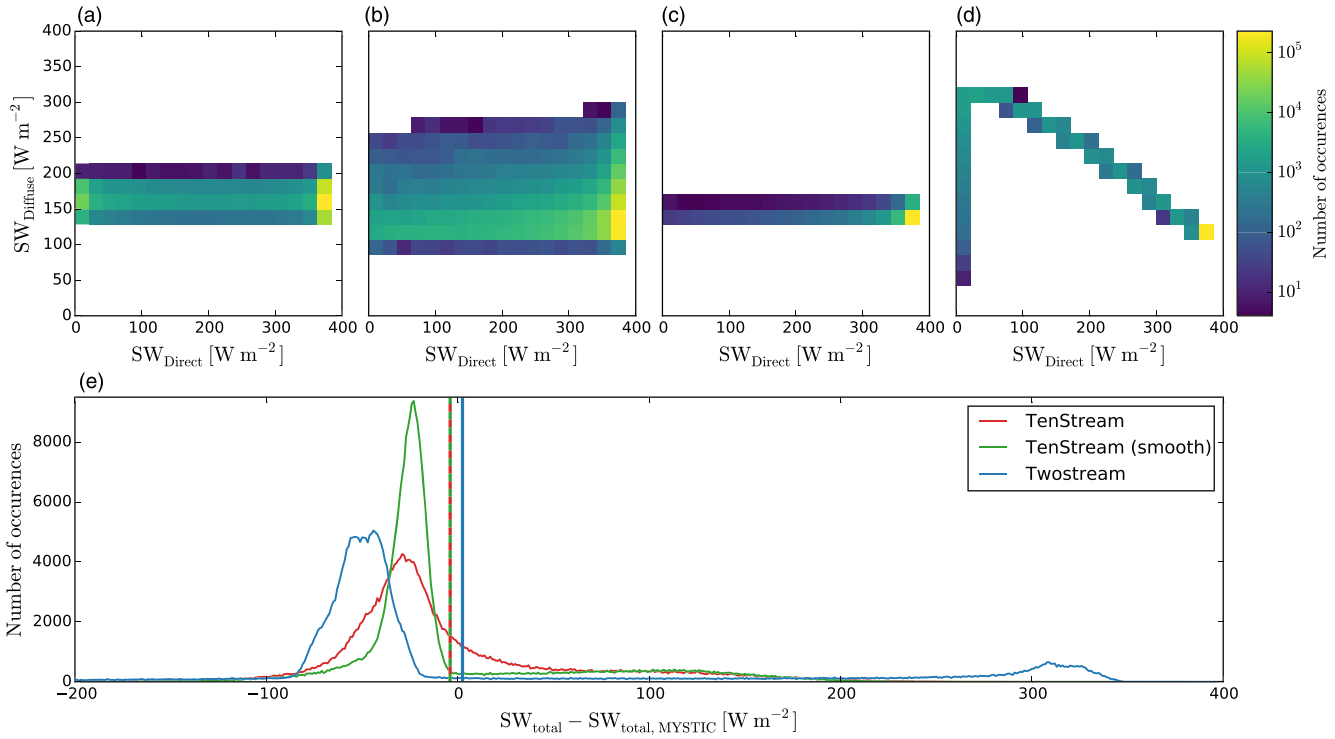

Figure 2. Two-dimensional histogram of direct and diffuse shortwave radiation at the surface summed over seven cloud fields, using MYSTIC (a), the TenStream solver (b), the TenStream solver with domain averaged diffuse radiation at the surface (c), a 1-D δ-Eddington two-stream solver (d), and histograms of the errors in the total shortwave radiation with respect to MYSTIC (e). The vertical lines in (e) show the domain average error. The cloud fields are taken from an independent numerical experiment, and a zenith angle of 60° was used. Note that the color scale is logarithmic due to the prevalance of clear sky patches. The upper left corner in (d) represents cloud optical depth of approximately 6–7.

vegetation (Jacobs & de Bruin, 1997; Jacobs et al., 1996; Ronda et al., 2001). This model depends on the PAR, which we approximate as 50% of the shortwave radiation reaching the surface. Additionally, we use the three-layer canopy radiative transfer scheme described by Pedruzo-Bagazgoitia et al. (2017). This canopy scheme treats the incoming diffuse radiation as isotropic but takes the solar zenith angle into account for the extinction rate of direct radiation. At each time step, this canopy scheme first calculates both the direct and diffuse shortwave fluxes at three canopy levels. The assimilation rate and stomatal resistance are then calculated at each level, which are subsequently upscaled to represent the whole canopy. This allows for an accurate response of the surface heat fluxes, in particular the partitioning between sensible and latent heat, to changes in incoming solar radiation. However, we assume that plants respond instantaneously to changes in environmental variables such as radiation. This leads to a stronger coupling between clouds and surface fluxes than with a more realistic response time of the vegetation (Sikma et al., 2018), but when wind speeds are low (<2.5 m s^{-1}) as in this study, we may expect that this stronger surface coupling has little impact on the surface fluxes or cloud cover (Sikma & Vilà-Guerau de Arellano, 2019).

Moreover, although leaves can scatter radiation in any direction and nonscattered radiation propagates through the canopy under the solar zenith angle, the canopy scheme only considers the vertical propagation of radiation within the canopy. Incorporating lateral radiative transfer into a 1-D canopy scheme (e.g., Hogan et al., 2018), or even explicitly computing the 3-D transfer of radiation inside the canopy (e.g., Kobayashi et al., 2012), can improve the simulated spatial distribution of radiation within the canopy. However, this will further increase computational costs. Given the high vegetation fraction and low vegetation type (see section 2.3), we are confident that our canopy scheme adequately represents the radiative transfer within the canopy.

2.3. Numerical Experiments

The initial and background conditions are based on the case used by Pedruzo-Bagazgoitia et al. (2017) and designed by Vilà-Guerau de Arellano et al. (2014). The case represents a late September day (day

of year: 268) in the Netherlands (51.97°N, 4.93°E) with shallow cumulus developing in the afternoon. We modified the case by increasing the initial specific humidity in the boundary layer, the soil moisture content, and the atmospheric stability in the upper part of the domain to delay the onset of midlevel clouds in simulations with 3-D radiative transfer. The initial and background profiles of temperature and moisture are based on observations from the Cabauw Experimental Site for Atmospheric Research (CESAR). The vegetation type is short grass, with a cover of 90% (the remaining 10% is bare soil) and a leaf area index of 2. The initial temperature and soil moisture content of the upper soil layer are 282 K and 0.455 $m^3\ m^{-3}$, respectively, so the soil is well watered and the grass does not experience any drought stress. There are no large-scale forcings and an all-or-nothing scheme with no precipitation is used for cloud microphysics, meaning that all moisture above the saturated moisture content instantly condensates. The size of the domain is $19.2 \times 19.2 \times 7.02\ km^3$, with periodic boundary conditions in horizontal direction and a resolution of $100 \times 100 \times 24\ m^3$. The 25% highest vertical layers form a sponge layer to prevent the reflection of fluctuations at the domain top (Heus et al., 2010). All simulations are run for 10 hr, starting at 7 UTC (09:00 local time), and the time step is adaptive based on the Courant-Friedrichs-Lewy (CFL) number, with a maximum of 20 s. The solar zenith angle follows a diurnal cycle, varying between 85.0° and 52.4°, and the azimuth angle varies from 107.0° to 261.1°. The radiation time step is 30 s, but only the rapidly changing spectral bands are recalculated at every time step due to the adaptive spectral integration. The full spectrum is only recalculated every 300 s. To account for radiative effects in the upper troposphere and stratosphere, we add, in the radiative transfer solvers, background profiles of temperature, humidity, ozone, carbon dioxide, methane, nitrous oxide, and oxygen on top of the domain.

Five different experiments are performed in total (Table 1). The two main experiments, using either RRTMG (`2-stream`) or the TenStream solver (`10-stream`) for radiation, are used to study the effects of 3-D radiative transfer on surface fluxes and cloud development compared to 1-D radiative transfer. The other experiments have the following aims. Jakub and Mayer (2015) already observed that the horizontal diffusivity of the TenStream solver is too low, which can result in surface areas with too much incoming diffuse radiation under clouds. To study the sensitivity of this effect, two additional experiments (`2-stream_smooth` & `10-stream_smooth`) are therefore performed, one with each radiative transfer solver, but with the longwave and diffuse shortwave radiation domain-averaged at the surface. This allows us to isolate the effects of changes in direct radiation due to clouds. The last experiment (`Transparent`) was performed with RRTMG, but with transparent clouds (i.e., cloud optical depth = 0) in the radiation scheme to obtain clear-sky radiative fluxes while still considering all dynamic effects of clouds. Although it is characterized by high direct solar irradiances, this experiment helps us to isolate the effects of the modulation of incoming radiation by clouds on the spatial distribution of the surface fluxes.

3. Numerical Performance

The large computational costs of full 3-D radiative transfer models heavily limits their use in numerical weather prediction and academic studies. It is therefore important to determine the additional computational time required for a 3-D radiative transfer solver compared to 1-D radiative transfer solvers. Jakub and Mayer (2015) already found that the TenStream solver is about 15 times slower than a δ-Eddington two-stream radiative transfer solver. Jakub and Mayer (2016) studied the scalability and numerical performance of the TenStream solver, coupled to the University of California Los-Angeles large-eddy simulation (UCLA-LES), in more detail and found that the runtime was only 5 to 10 times higher. An extensive analysis of the performance of the TenStream solver is therefore out of the scope of this study, but we provide an overview of the computational costs of the TenStream solver in our simulations.

The `10-stream` and `2-stream` simulations were run on the Dutch national supercomputer Cartesius using 256 cores distributed over 11 compute nodes (2 × 12-core Intel Xeon E5-2690 v3, 2.6 GHz, 64 GB memory). Including the background profile of 48 levels representing the upper atmosphere, the workload per core is thus $12 \times 12 \times 342$ grid cells per core. The total wall clock time of the `2-stream` simulation was about 3,996 s, whereas the `10-stream` simulation finished in 52,980 s, which is roughly a factor of 13 slower. However, individual radiation time steps are often well over 2 orders of magnitude more expensive with the TenStream solver than with RRTMG. Due to the adaptive spectral integration, intermediate radiation

Table 2
Elapsed WCT of the TenStream Simulations, Normalized to the `2-stream` *Simulations ($WCT_{TenStream}/WCT_{RRTMG}$ [−]), in Clear Sky and Cloudy Conditions, for the Time Spent in the Radiation Schemes Only and for the Total Simulation Time*

	Radiation	Total
Clear sky	210.9	25.8
Cloudy	226.1	12.2

Note. WCT = wall clock times. Simulations were run for 1 hr (model time), with a radiation time step of 300 s.

time steps can be faster especially if clouds are not yet present, which explains the relatively lower difference in total wall clock time.

To get a better overview of the difference in runtime between the TenStream solver and RRTMG in our experiments, we perform two small additional simulations with each radiative transfer solver: one with only clear sky and one with clouds already present. For these simulations, we use just one node (24 cores), but with the same workload (12 by 12 vertical columns) per core as the main experiments. The simulations are run for 1 hr, and radiation is called every 300 s, without adaptive spectral integration.

The computational costs of the TenStream solver are almost 211 times larger than the computational costs of RRTMG for clear-sky computations and about 226 times larger with clouds (Table 2). This increase in computational costs is much larger than the 5–10 increase in computational costs reported by Jakub and Mayer (2016). This much larger increase in runtime is partly due to the diurnal cycle used in this study, which results in rapidly changing solar zenith angles between radiation time steps. Other possible explanations are differences between the performance of RRTMG and of the 1-D radiative transfer solver used by Jakub and Mayer (2016), insufficiently optimized matrix preconditioner and solvers (Jakub & Mayer, 2016), differences in the hardware used for benchmarking, and differences in the vertical resolution and domain height. The runtime of the total simulation is about 12 times larger with the TenStream solver if clouds are present, but almost 26 times larger under clear sky. However, enabling the adaptive spectral integration can strongly reduce the extra computational costs of the TenStream solver if clouds are absent, since not all spectral bands have to be recomputed at each radiation time step. Intermediate radiation time steps can therefore be over 2 orders of magnitude faster.

4. Results and Discussion

4.1. Shallow Cumulus Development Over an Interactive Surface

Figure 3 shows the diurnal cycle of the cloud cover, LWP, and the boundary layer height in the five experiments. The cloud covers in the `2-stream` and `10-stream` experiments develop similarly until about 15 UTC, but afterward, the cloud cover in the `10-stream` experiment increases to about 0.25, whereas the clouds in the `2-stream` experiment dissipate in the late afternoon, in accordance to a shallow cumulus

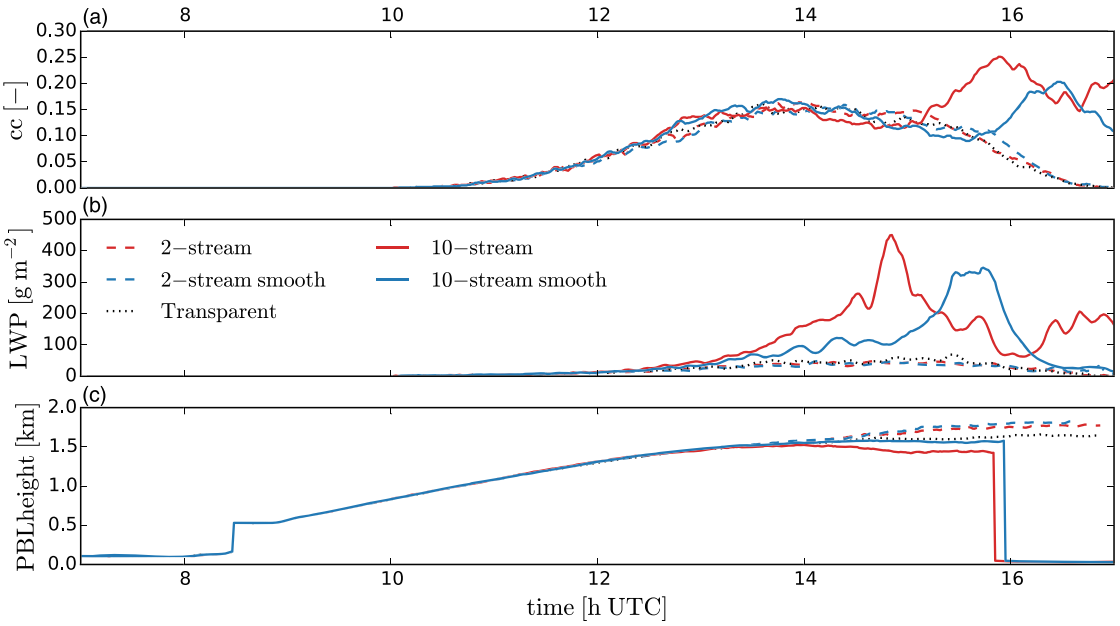

Figure 3. Time series of the cloud cover (a), the liquid water path averaged over only cloudy columns (b), and the domain-averaged boundary layer height (c).

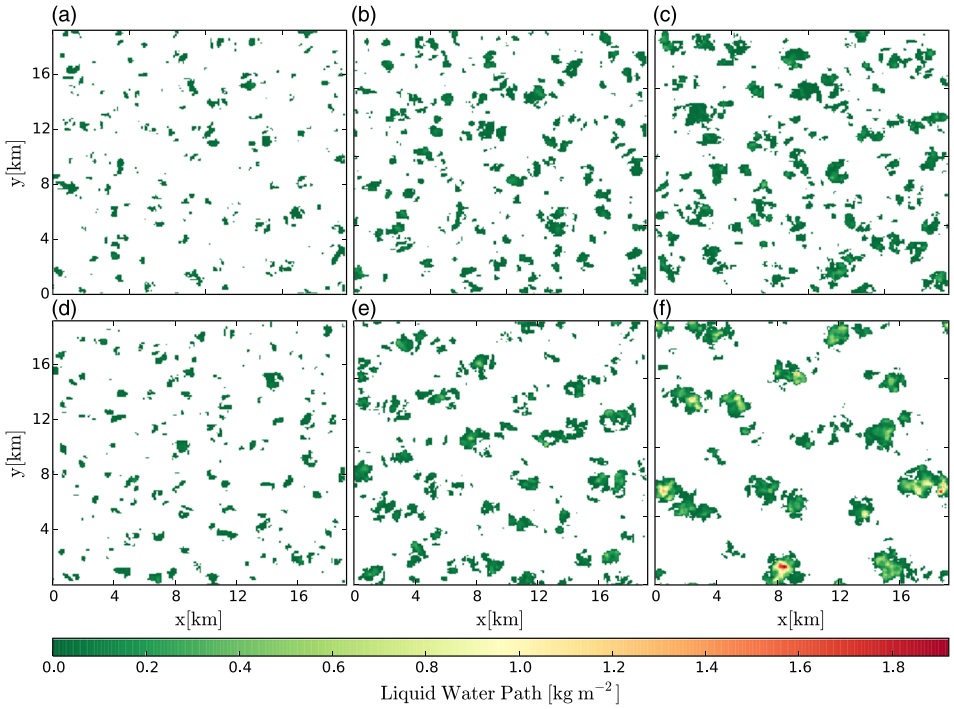

Figure 4. Horizontal cross sections of the intantaneous liquid water path at 12 UTC (a and d), 13 UTC (b and e), and 14 UTC (c and f) for the `2-stream` (a–c) and `10-stream` (d–f) experiments.

situation, which prevents the triggering of deep convection. Despite the similar cloud cover up to 15 UTC, we can already observe differences in size and thickness of individual clouds between the `2-stream` and `10-stream` experiments (Figure 4). The LWP in the afternoon is also much larger in the `10-stream` experiment than in the `2-stream`experiment. The difference in LWP is generally larger than the difference in cloud cover (around 14 UTC, the cloud cover is approximately equal, whereas the LWP is about four times higher in `10-stream` than in `2-stream`), which suggests that clouds become thicker with 3-D radiative transfer.

We attribute these differences in LWP mainly to the differences in the spatial distribution of the solar radiation at the surface underneath clouds (Gronemeier et al., 2017; Jakub, 2016). Due to the displaced cloud shadows in the `10-stream` experiment, the direct shortwave radiation is often not reduced below clouds, while the diffuse radiation is still enhanced compared to clear-sky conditions (Table 3). In the `2-stream` experiment, the decrease in direct radiation below clouds is larger than the increase in diffuse radiation (Table 3), resulting in less shortwave radiation reaching the surface below clouds than in the `10-stream` experiment. This leads to a weakening of the turbulent thermals below clouds and a reduction of the turbulent transport of heat and moisture (Vilà-Guerau de Arellano et al., 2014; Horn et al., 2015), resulting in faster dissipating clouds. In the `10-stream` experiments, the surface heat fluxes are enhanced below clouds, continuously supplying energy and moisture to the clouds (Jakub & Mayer, 2017). Additionally, the displaced cloud shadows may generate secondary circulations that can contribute to the larger clouds in the `10-stream` experiment (Gronemeier et al., 2017; Jakub & Mayer, 2017). Another possible cause of the different cloud evolution may be differences in radiative heating. Horizontally averaged over all grid cells containing liquid water, we find slightly stronger longwave cooling and shortwave warming rates in the `2-stream` experiment (not shown), presumably due the the different vertical extents of the clouds in the `2-stream` and `10-stream` experiment. However, we expect that this difference in radiative heating rates has little effect compared to the different surface distribution of solar radiation, especially on the short (diurnal) time scales in this study (Klinger et al., 2017).

The differences in cloud cover between the `10-stream` and `2-stream` experiments after 15 UTC are larger than the differences in cloud cover found by Wapler (2007) and Jakub (2016) between simulations with 1-D

Table 3
The Total SW_{tot}, Direct SW_{dir}, and Diffuse SW_{dif} Downward Shortwave Radiative Fluxes (W m^{-2}); the Upward LW_{up} and Downward LW_{dn} Longwave Radiative Fluxes (W m^{-2}); the Surface Sensible (H) and Latent (LE) Heat Flux (W m^{-2}), and the CO_2 Assimilation Rate (An) (μg m^{-2} s^{-1}) at the Surface, Averaged Over the Whole Domain (Full) and Conditionally Averaged Over Only Clouded (Cloudy) and Nonclouded (Clear-Sky) Areas

		SW_{dir}	SW_{dif}	SW_{tot}	LW_{up}	LW_{dn}	H	LE	An
10-stream	Full	520	81	602	418	299	110 (+2%)	193 (+2%)	−589 (+1%)
	Cloudy	530	135	665	423	313	131 (+40%)	217 (+16%)	−641 (+6%)
	Clear sky	519	75	595	418	297	108 (−1%)	191 (0%)	−584 (+1%)
_smooth	Full	524	80	603	418	298	111 (+3%)	193 (+2%)	−590 (+1%)
	Cloudy	530	81	612	418	299	116 (+24%)	198 (+6%)	−599 (−1%)
	Clear sky	523	79	602	418	298	110 (+1%)	193 (+1%)	−589 (+2%)
2-stream	Full	532	71	603	417	291	108	190	−582
	Cloudy	246	241	487	416	333	93	187	−605
	Clear sky	558	56	614	417	287	109	190	−580
_smooth	Full	534	70	604	417	291	110 (+2%)	189 (0%)	−574 (−1%)
	Cloudy	253	71	324	417	291	56 (−40%)	118 (−37%)	−393 (−35%)
	Clear sky	558	70	628	417	291	114 (+5%)	195 (+3%)	−590 (+2%)
Transparent	Full	558	56	613	418	288	110 (+2%)	191 (0%)	−580 (0%)

Note. Fluxes are averaged between 12 and 13 UTC, similar to Figure 3. Between parentheses are the relative changes compared to 2-stream full, cloudy, or clear sky, respectively. The averaged fluxes in this table are indicative. Local values depend heavily on the thickness and spatial distribution of clouds.

and 3-D radiative transfer. This larger cloud cover is mainly due to a cloud layer developing at approximately 4 km height, presumably due to horizontal spreading of the much more buoyant plumes in the 10-stream experiment (Figure 5) below a more stable layer. Another plausible cause for the horizontal spreading might be that precipitation is disabled. Precipitation may lead to lower cloud covers and LWPs by removing water from the atmosphere but could also induce cold-pool dynamics (Schlemmer & Hohenegger, 2014) that result in larger clouds, further complicating the relation between radiation and cloud development. However, a thorough study of this cloud layer is out of the scope of this work, and therefore, we focus the rest of this research on the first half of the simulations (up to 14 UTC).

The CO_2 uptake is enhanced underneath clouds in both experiments (Table 3). The enhancement in the 10-stream experiment is not surprising given the higher shortwave fluxes below clouds. The enhanced assimilation rate in the 2-stream experiment is due to the diffuse enhancement effect below optically thin clouds, as has also been found by Pedruzo-Bagazgoitia et al. (2017) and Sikma et al. (2018). Such an enhancement below clouds in the 2-stream experiment is also found for the latent heat flux (see section 4.2), but weaker and only for cloud optical depths below 4. Since diffuse radiation can penetrate deeper into the

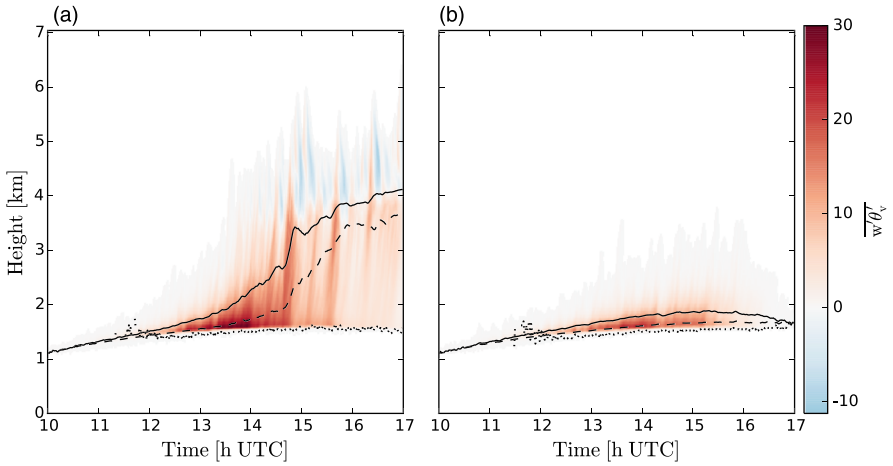

Figure 5. Height-time plots of the vertical virtual potential temperature flux, averaged over only grid cells containing liquid water, in the 10-stream (a) and the 2-stream (b) experiments. Solid and dashed lines denote the average cloud top and cloud base, respectively. Dotted lines denote the minimum base of only positively buoyant clouds.

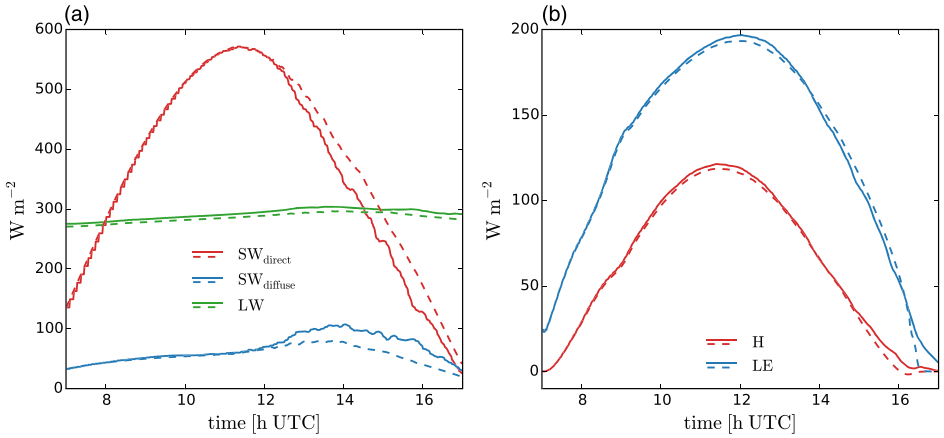

Figure 6. Time series of (a) the downwelling diffuse SW$_{diffuse}$ and direct SW$_{direct}$ shortwave and downwelling longwave LW radiation at the surface and (b) the surface latent (LE) and sensible (H) heat fluxes in the `10-stream` (solid lines) and `2-stream` (dashed lines) experiments.

canopy than direct radiation, the available light is distributed more evenly over the canopy, which enhances the rate of photosynthesis of the canopy (Kanniah et al., 2012; Li et al., 2014). However, the domain-averaged CO_2 uptake in the `10-stream` and `2-stream` experiments is very similar, indicating that the differences in the CO_2 uptake under clear sky and under clouds between both experiments compensate each other.

In both experiments, the downward longwave radiation at the surface is also enhanced beneath clouds (Table 3). However, the differences in longwave radiation between cloudy and clear-sky regions are on average about four times lower than the differences in shortwave radiation. Additionally, the assimilation rate and latent heat flux depend mainly on shortwave radiation because plants respond mostly to changes in shortwave radiation by changing the aperture of their stomata, which affects the stomatal resistance of the canopy. For these reasons, from now on we focus only on shortwave radiation in this study, although we simultaneously account for the effects of both shortwave and longwave radiation.

The domain-averaged radiative fluxes in the `2-stream` and `10-stream` experiments are quite similar up to about 15 UTC, although the longwave flux is slightly higher in the `10-stream` experiment (Figure 6). In the afternoon, the direct (diffuse) shortwave radiation in the `10-stream` experiment becomes lower (higher) than in the `2-stream` experiment. The surface heat fluxes are nevertheless quite similar, indicating the increase in diffuse and decrease in direct radiation partially compensate. In `10-stream`, the total shortwave radiation is on average about 1 W m^{-2} lower than in `2-stream` between 12 and 13 UTC, but around 20 W m^{-2} lower at 14 UTC. The lower total shortwave radiation may be attributed to the higher and thicker clouds in `10-stream` leading to more scattering, but also to pure 3-D radiative effects: Even for identical cloud fields, Gristey et al. (2020) already found lower surface irradiances with 3-D radiative transfer compared to 1-D radiative transfer.

To connect these surface forcings to the development of the boundary layer, we define the ABL height as the first height at which the vertical gradient of the virtual potential temperature (θ_v) equals 50% of the maximum θ_v gradient in the lowest 3,500 m (Ouwersloot et al., 2011). The ABL height develops quite similarly in both experiments in the first half of the simulation. In the afternoon, the growth of the ABL is slower in the `10-stream` experiment, likely due to the lower sensible heat fluxes. Around 1600 UTC, the ABL height rapidly drops in the `10-stream` experiment due to a relatively strong inversion near the surface (not shown), which is presumably caused by the low solar irradiance as a result of the high cloud cover.

Given the insufficient diffusivity of the TenStream solver and the absence of horizontal radiative transfer in RRTMG, smoothening the diffuse radiation at the surface is a way of improving or accounting for horizontal diffusion of radiation (Wissmeier et al., 2013; Zuidema & Evans, 1998). This smoothening therefore reduces the diffuse radiation below clouds, especially with 1-D radiative transfer (`2-stream` and `2-stream smooth`). Despite the lower radiative fluxes below clouds, the differences in cloud cover, LWP, and PBL height between the `2-stream` and `2-stream_smooth` experiments are rather small.

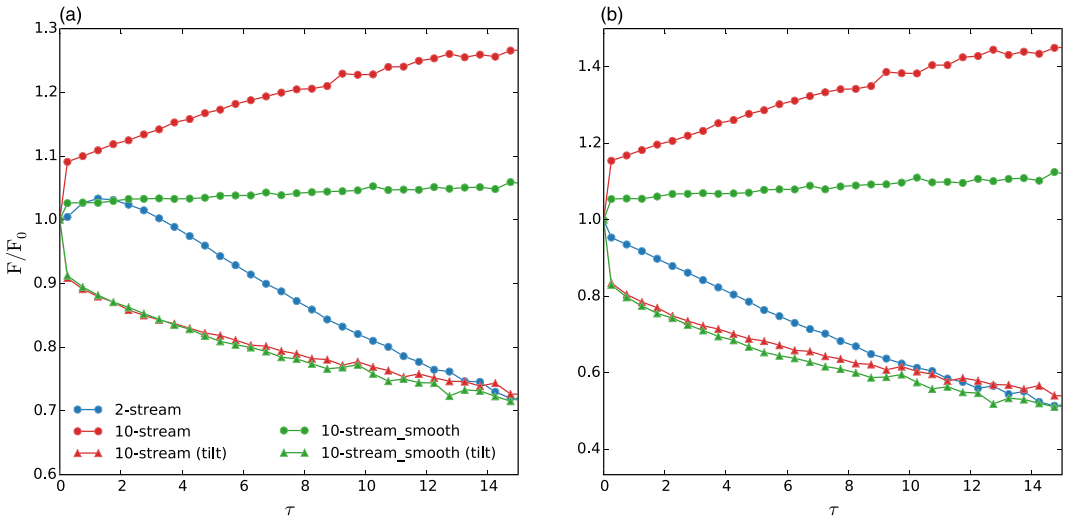

Figure 7. Mean latent (a) and sensible (b) heat fluxes as a function of optical depth (τ) bin, averaged between 12 and 13 UTC and normalized by the clear sky ($\tau = 0$) flux, for the `2-stream`, `10-stream`, and `10-stream_smooth` experiments with τ calculated along a vertical path and for the `10-stream` and `10-stream_smooth` experiments also with the optical depth calculated along the slanted path of sunrays (tilt).

The strong increase in cloud cover and LWP in the later afternoon is still observed in the `10-stream_smooth` experiment, although the peaks are lower and occur about 30–60 min later. This suggests that the impact of the low diffusivity of the TenStream solver is relatively small and that the removal of part of the clouds shadows below clouds is sufficient to strongly modify the size and optical thickness of the clouds.

4.2. Spatial Heterogeneity of Surface Fluxes

The coupling between surface and clouds is bidirectional. Since clouds can scatter and absorb more of the incident solar radiation as they thicken, the total incoming shortwave radiation and the partition between direct and diffuse radiation after the cloud depend on cloud thickness (Pedruzo-Bagazgoitia et al., 2017). As a result, the local surface heat fluxes are influenced by the thickness of clouds directly above and, with 3-D radiative transfer, of surrounding clouds. In turn, the surface heat fluxes affect the growth and thickness of clouds by providing heat and moisture to the clouds (Vilà-Guerau de Arellano et al., 2014). It is therefore interesting to study the spatial distribution of the surface heat fluxes in the presence of clouds in more detail.

To investigate the response of the surface heat fluxes to clouds thickness, we calculate the cloud optical depth (τ) from LWP following Stephens (1978)

$$\tau = \frac{3}{2\rho_w r_{eff}} \frac{1}{\int_I w_c \, ds},$$

with density of water ρ_w (1,000 kg m^{-3}), effective droplet radius r_{eff}, and liquid water content w_c (in kg m^{-3}). The integral is the LWP along path I between the surface and the domain top.

We then divide local values of H and LE into bins according to τ and subsequently average H and LE per bin between 12 and 13 UTC. The bins have a width of 0.5, but we use a separate bin for τ=0. For the `2-stream` experiment, we calculate τ along a vertical path, corresponding to the vertical propagation of radiation with 1-D radiative transfer. For the `10-stream` and `10-stream_smooth` experiments, we calculate τ both along a vertical path and along the slanted path of sunrays (`10-stream` [tilt], `10-stream_smooth`[tilt]), depending on the solar zenith angle. Given the mean zenith angle of 54.5° and mean cloud base of 1,491 m between 12 and 13 UTC, the distance between a cloud and its shadow is about 2,098 m.

In the `2-stream` experiment, the sensible heat flux decreases continuously with increasing τ (Figure 7). The latent heat flux also decreases with increasing τ for optical depths above 2. For lower optical depths (τ<2), LE

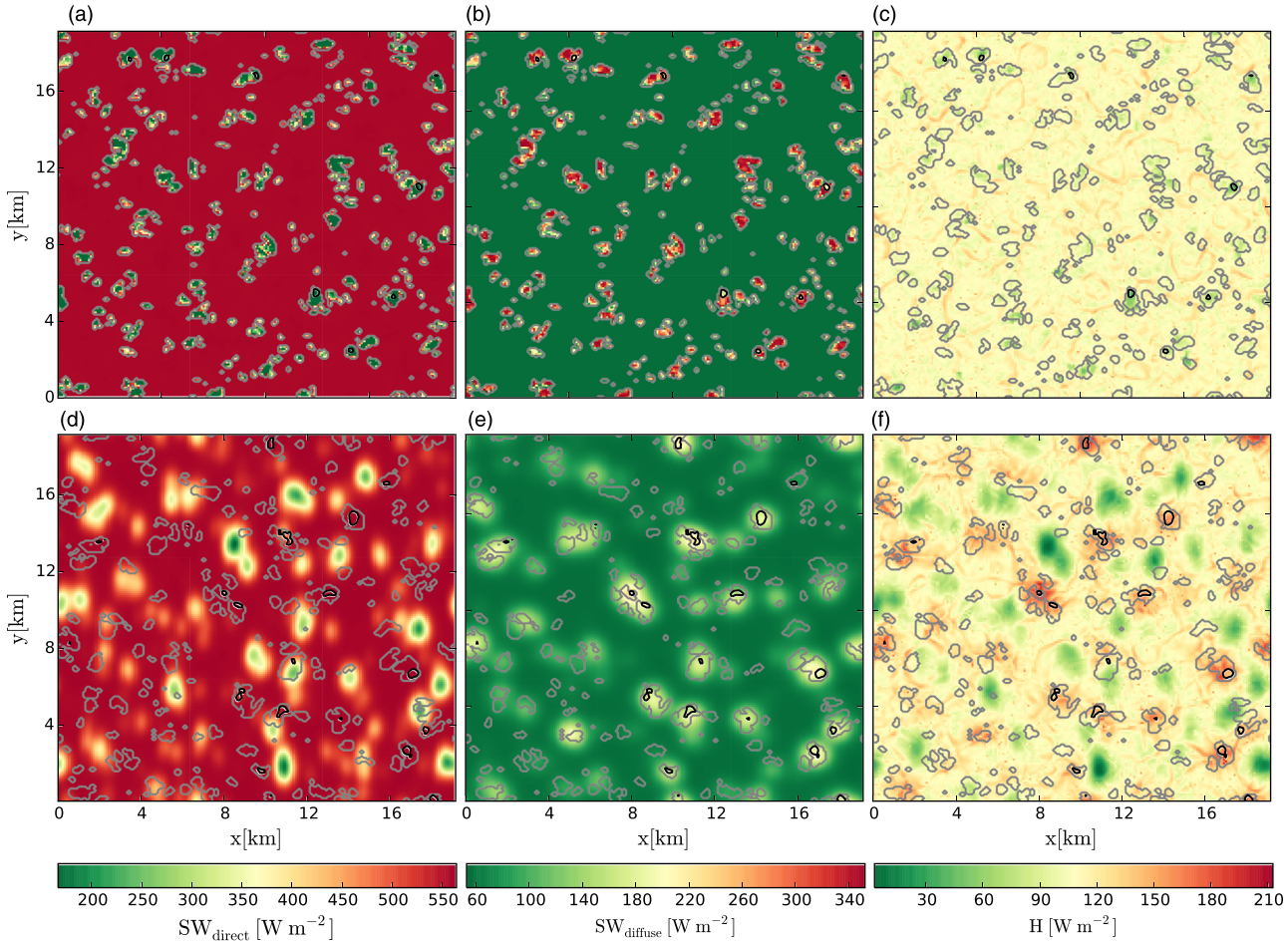

Figure 8. Horizontal cross sections of the intantaneous direct (a and d) and diffuse (b and e) downward shortwave radiation at the surface and the sensible heat flux (c and f), for the `2-stream` (a–c) and `10-stream` (d–f) experiments, at 12:30 UTC (zenith angle = 54°). The zenith angle gray and black contours show all clouds (τ>0) and only thick clouds (τ>15), respectively.

increases as τ increases, which corresponds to the enhanced LE regime under thin clouds found by Pedruzo-Bagazgoitia et al. (2017) and Sikma et al. (2018). This LE enhancement under thin clouds is a result of the conversion from direct to diffuse radiation by clouds, which leads to more photosynthesis and therefore more evapotranspiration despite the decrease in total shortwave radiation. In both the `10-stream` and `10-stream_smooth` experiments, H and LE decrease similarly with increasing optical depth if we calculate τ along the slanted path of sunrays (`10-stream` [tilt], `10-stream_smooth` [tilt]; Figure 7), although the surface heat fluxes are slightly lower in the `10-stream_smooth` experiment for τ>4. This indicates the dominant role of the decrease in direct radiation with increasing τ over the enhanced diffuse radiation below cloud. H and LE are lower in `2-stream` than in `10-stream` and `10-stream_smooth` beneath clouds with optical depths up to about 15, but higher underneath thicker clouds due to the limited enhancement of diffuse radiation below thick clouds in combination with the slightly smoother cloud shadows in the TenStream solver (Figure 8; Jakub & Mayer, 2015)

In `2-stream` and `10-stream`, the diffuse radiation at the surface depends mostly on the clouds above due the vertical propagation of radiation in RRTMG and the insufficient diffusivity of the TenStream solver (see section 2.3; Jakub & Mayer, 2015). If τ is calculated along a vertical path, both surface heat fluxes rapidly increase with increasing optical depth (Figure 7) in `10-stream`: Thicker clouds can scatter more diffuse radiation downward but do not reduce the incoming direct radiation at the surface beneath it due to the tilted path of the sunrays (Figures 8d and 8e). Given this dependency on the diffuse radiation, it is not surprising that the surface flux increases only slightly with increasing vertical τ in `10-stream_smooth`. In

fact, rather than to 3-D radiative effects, this signal may perhaps be attributed to the spatial distribution of clouds, such as a larger likelihood for the surface below thin clouds to be shaded by surrounding clouds, or a more frequent occurrence of thick clouds later in the averaging period, when the solar elevation angle and thus the direct shortwave clear-sky flux are larger.

Whereas with 1-D radiative transfer, the reduced direct radiation below clouds is partially compensated by an increase in diffuse radiation (Figures 8a and 8b), the displaced cloud shadows with 3-D radiative transfer result in patches where the direct and diffuse radiation are both low or both high (Figures 8d and 8e). For example, the reflection of radiation by clouds onto sunlit patches may results in local irradiances exceeding clear-sky irradiances, as is also known from field observations (e.g., Franceschini, 1968; Segal & Davis, 1992). Comparing Figure 8 to the Monte Carlo computations of Gristey et al. (2020) also indicates again that the TenStream solver is insufficiently diffusive but produces smoothed cloud shadows due to numerical diffusion (section 2.1; Jakub & Mayer, 2015). The contrasts in total shortwave radiation and therefore the surface heat fluxes between clouded and clear-sky patches become larger with 3-D radiative transfer than with only vertically propagating radiation (Figures 8c and 8f). This indicates that the dynamic heterogeneities caused by cloud shading are more dominant with 3-D radiative transfer than with 1-D radiative transfer. In the `10-stream` and `10-stream_smooth` experiments, we may therefore expect stronger spatial variabilities in the surface heat fluxes and possible larger thermal structures originating at the surface due the larger spatial extent of patches with high surface heat fluxes. It must be noted, however, that our results are based on a case study and should be tested for generalizability across multiple cases in the future.

To quantify and further investigate the spatial variability of the sensible heat fluxes, we use a 2-D forward Fourier transformation in both horizontal directions to spectrally decompose the sensible heat flux at each time step and subsequently calculate spectral densities following Horn et al. (2015). Based on the calculated spectra, we also calculate the characteristic length scale of the spatial variability in H following the definition given by Pino et al. (2006, Equation 3)

$$\frac{\int_0^\infty S_H(k)k^{-1}dk}{\int_0^\infty S_H(k)dk},$$

where S_H is the spectral density of H at each wave number k. Since we are interested in how variations in the sensible heat flux influence atmospheric turbulence and cloud dynamics, we also calculate spectral densities and characteristic length scales of the LWP and the vertical velocity (w) at a height of 540 m, about one third of the boundary layer height, where we expect strong vertical velocity fluctuations (Sullivan & Patton, 2011).

The spectral densities and power spectra (Figure 9) are a quantification of the spatial variability of the liquid water path and sensible heat flux shown in Figures 8c and 8f. In the `2-stream` experiment, the peak of the power spectrum is shifted to lower wave numbers, and the total variance of H is higher than in the `Transparent` experiment, in which the clouds are considered transparent (τ=0) in the radiation scheme (Figure 9a). Around 12:30 UTC, the dominant length scale of H is about 1,150 min the `2-stream` experiment, which is approximately two thirds of the boundary layer height (Figure 3c), and only about 850 min the `Transparent` experiment (Figure 9b). These differences can be attributed to the presence of clouds in the `2-stream` experiment, since the characteristic length scales start diverging around 11 UTC (Figure 9b), when the clouds are developing (Figure 3). The total variance of the LWP is higher in the `Transparent` experiment than in the RRTGM experiment (Figure 9c), which is presumably due to the higher available energy at the surface in the absence of cloud shading, leading to slightly thicker clouds (Horn et al., 2015). The length scales of the LWP and w are approximately similar in the `2-stream` and `Transparent` experiments (Figures 9b and 9c), also later in the afternoon (after 13 UTC) despite some temporal fluctations (Figures 9e and 9f).

The total variance of H is much higher in the `10-stream` and `10-stream_smooth` experiments than in the `2-stream` experiment (Figure 9a), which shows that using 3-D radiative transfer increases the spatial variability of H due to the large patches underneath clouds with higher H than under clear sky that are not present in the `2-stream` experiment (Figure 8). The power spectral density peaks at smaller wave numbers and the characteristic length scales are much larger in the `10-stream` experiment, about twice the

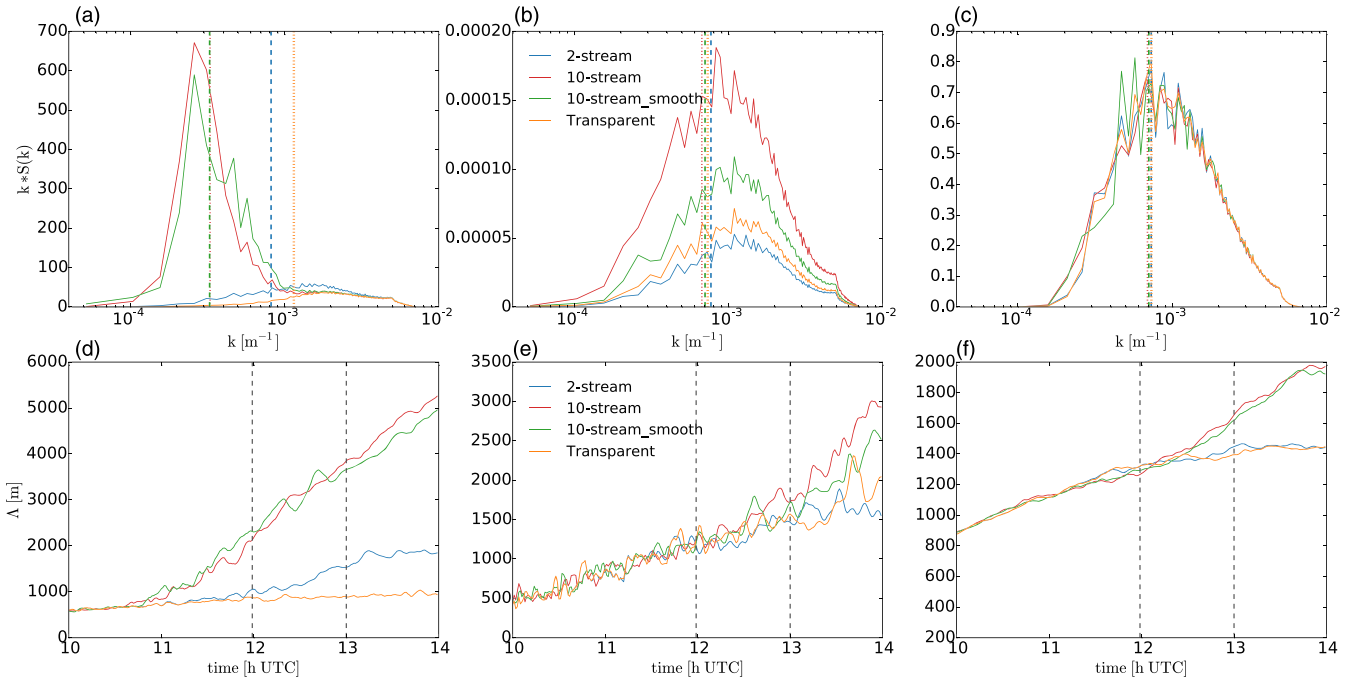

Figure 9. Power spectral density S(k) of (a) sensible heat flux (H), (b) liquid water path (LWP), and (c) vertical wind velocity (w) at 540 m, scaled with wave number k and averaged between 12 and 13 UTC, and time series of the characteristic length scales Δ of (d) H, (e) LWP, and (f) w for the `2-stream`, `10-stream`, `10-stream_smooth`, and `Transparent` experiments. The area under the curves in a, b, and c is equal to the total variance of H, LWP, and w, respectively. The vertical lines in a, b, and c (dotted for `10-stream` and `Transparent`, dashed for `10-stream_smooth` and `2-stream`) represent the mean characteristic length scales, averaged between 12 and 13 UTC, and the vertical lines in d, e, and f show the averaging period.

boundary layer height around 12 UTC (Figure 9b), and rapidly increase later in the afternoon. The characteristic length scales of the LWP and w are also larger in the `10-stream` and `10-stream_smooth` experiment, and the spectral density of w is higher at the smallest wave numbers. However, the difference in the length scale between the `10-stream` experiments and the experiments with 1-D radiation is smaller for LWP and w than for H. This indicates that the length scales of H are mainly driven by the surface distribution of radiation, whereas the length scales of w are largely constraint by the boundary layer height (Jonker et al., 1999) and the length scales of LWP by the available moisture and the temperature.

The larger length scales of the LWP and w in the `10-stream` and `10-stream_smooth` experiment may suggest that, with 3-D radiative transfer, larger convective thermals dominate the turbulent structure of the boundary layer, mainly because the surface fluxes beneath clouds are not reduced by cloud shading but enhanced compared to clear-sky fluxes. Additionally, the length scales of the vertical motions may also be dominated by the presence of secondary circulations, which can be generated by the displacement of clouds shadows (Gronemeier et al., 2017) or the difference in solar radiative heating between the sunlit and shadowed sides of clouds (Jakub, 2016).

5. Conclusions

We coupled a 3-D radiative transfer solver to a large-eddy simulation model and performed a case study to investigate the impact of 3-D radiative effects on the coupling between clouds, solar radiation, and the vegetated land surface. Our main focus is on the dynamic heterogeneities in direct and diffuse solar irradiance and in the subsequent surface heat fluxes due to the absorption and scattering of solar radiation by clouds. To this end, we performed multiple large-eddy simulations, using either a 1-D or a 3-D radiative transfer solver, of a convective boundary layer over grassland with shallow cumulus clouds developing in the afternoon.

Although the differences in the domain-average surface heat fluxes are less than 3 W m^{-2}, the sensible and latent heat fluxes below clouds are on average 38 and 30 W m^{-2} larger, respectively, with 3-D radiative

transfer than with 1-D radiative transfer, and even larger than the clear-sky surface heat fluxes. We attribute this to the horizontally shifted cloud shadows when the Sun is not directly overhead in combination with the increase in diffuse radiation below clouds. As a result of this larger net available energy at the surface, we find that simulations with 3-D radiative transfer develop much thicker clouds with larger LWPs than simulations with 1-D radiative transfer, even when diffuse irradiance fields are smoothened by horizontally averaging the diffuse radiation at the surface. This indicates that the displacement of clouds shadows with 3-D radiation is sufficient to strongly modify the development of the cloud field.

To further investigate dynamical heterogeneities due to clouds and the subsequent effect on boundary-layer dynamics, we study the surface heat fluxes beneath clouds for different cloud optical depths. Furthermore, we determine the dominant length scales of the sensible heat flux, the LWP, and the vertical velocity in the middle of the boundary layer. With 1-D radiative transfer, the surface heat fluxes below clouds decrease with increasing cloud thickness, except for the enhanced latent heat fluxes beneath optically thin clouds. With 3-D radiative transfer, the surface heat fluxes below clouds increase with increasing cloud thickness. In cloud-shaded patches, however, the surface heat fluxes with 3-D radiative transfer decrease more rapidly with increasing cloud thickness than with 1-D radiative transfer and show no enhancement beneath thin clouds because of the low diffuse irradiance when no clouds are overheads. Due to the lower surface fluxes in cloud-shaded patches and higher surface fluxes beneath clouds, the spatial variability of the sensible heat flux with 3-D radiative transfer is dominated by much larger length scales, around 12 UTC more than twice as large as with 1-D radiative transfer. The dominant length scales of the vertical velocity and w are also larger with 3-D radiative transfer, suggesting that accounting for 3-D radiative effects may lead to larger thermal structures.

Although this study shows that 3-D radiative transfer can significantly affect the spatial distribution of the surface heat fluxes in the presence of clouds and the dominant length scales of thermals and clouds, our results are based on a single case study (Vilà-Guerau de Arellano et al., 2014; Pedruzo-Bagazgoitia et al., 2017). Different background conditions, such as changes in vegetation (Vilà-Guerau de Arellano et al., 2014), surface heat capacity (Jakub & Mayer, 2017), or wind speed (Sikma et al., 2018) may affect the interactions between radiation, clouds, and the surface fluxes. The coupling between the surface and individual clouds weakens as the wind speed increases (Sikma & Vilà-Guerau de Arellano, 2019), but even at high wind speeds (10 m s^{-1}), we can expect a strong coupling between the land surface and clouds on a regional scale (Jakub & Mayer, 2017; Sikma & Vilà-Guerau de Arellano, 2019). Aerosols also impact the surface solar irradiance by scattering and absorbing sunlight, which affects the surface heat fluxes and the evolution of the ABL (Barbaro et al., 2014). It is therefore recommended for future studies to investigate the impact of 3-D radiative effects for various environmental conditions to test the generalizability of our results. Furthermore, our results show that 3-D radiative transfer leads to more energetic thermals and a higher upward transport of moisture within the cloud layer, which presumably led to the spreading of cloud tops around 4 km height. It would be interesting to determine to what extent the development of such a midlevel cloud layer can be observed in different convective cases.

Data Availability Statement

The versions of DALES and the TenStream solver used for this study can be downloaded from https://doi.org/10.5281/zenodo.3830782 and https://doi.org/10.5281/zenodo.3830784, respectively. The data and scripts used to make the figures in this paper are available online (at https://doi.org/10.4121/uuid:91250c8f-8be4-4aeb-9238-9670499d8779).

Acknowledgments

This work was carried out on the Dutch national e-infrastructure with the support of SURF Cooperative, Project 16666. Chiel van Heerwaarden acknowledges funding from the Duth Research Council (NWO), Project VI. Vidi.192.068. Menno Veerman would like to thank Bernhard Mayer from the Meteorological Institute of the Ludwig Maximilian Universität (LMU) München for providing an internship and assisting with implementing the TenStream solver in DALES and testing this implementation.

References

Barbaro, E., Vilà-Guerau de Arellano, J., Ouwersloot, H. G., Schrter, J. S., Donovan, D. P., & Krol, M. C. (2014). Aerosols in the convective boundary layer: Shortwave radiation effects on the coupled land-atmosphere system. *Journal of Geophysical Research: Atmospheres*, *119*, 5845–5863. https://doi.org/10.1002/2013JD021237

Clough, S. A., Iacono, M. J., & Moncet, J.-L. (1992). Line-by-line calculations of atmospheric fluxes and cooling rates: Application to water vapor. *Journal of Geophysical Research*, *97*(D14), 15,761–15,785. https://doi.org/10.1029/92JD01419

Clough, S. A., Shephard, M. W., Mlawer, E. J., Delamere, J. S., Iacono, M. J., Cady-Pereira, K., et al. (2005). Atmospheric radiative transfer modeling: A summary of the AER codes. *Journal of Quantitative Spectroscopy and Radiative Transfer*, *91*(2), 233–244. https://doi.org/10.1016/j.jqsrt.2004.05.058

Emde, C., Buras-Schnell, R., Kylling, A., Mayer, B., Gasteiger, J., Hamann, U., et al. (2016). The libRadtran software package for radiative transfer calculations (Version 2.0.1). *Geoscientific Model Development*, *9*(5), 1647–1672. https://doi.org/10.5194/gmd-9-1647-2016

Franceschini, G. A. (1968). The influence of clouds on solar radiation at sea. *Deutsche Hydrografische Zeitschrift*, *21*(4), 162–168.
Fu, Q., & Liou, K. N. (1992). On the correlated k-distribution method for radiative transfer in nonhomogeneous atmospheres. *Journal of the Atmospheric Sciences*, *49*(22), 2139–2156. https://doi.org/10.1175/1520-0469(1992)049<2139:OTCDMF>2.0.CO;2
Gristey, J. J., Feingold, G., Glenn, I. B., Schmidt, K. S., & Chen, H. (2020). Surface solar irradiance in continental shallow cumulus fields: Observations and large-eddy simulation. *Journal of the Atmospheric Sciences*, *77*(3), 1065–1080. https://doi.org/10.1175/JAS-D-19-0261.1
Gronemeier, T., Kanani-Sühring, F., & Raasch, S. (2017). Do shallow cumulus clouds have the potential to trigger secondary circulations via shading? *Boundary-Layer Meteorology*, *162*(1), 143–169. https://doi.org/10.1007/s10546-016-0180-7
Heus, T., van Heerwaarden, C. C., Jonker, H. J. J., Pier Siebesma, A., Axelsen, S., vanden Dries, K., et al. (2010). Formulation of the Dutch Atmospheric Large-Eddy Simulation (DALES) and overview of its applications. *Geoscientific Model Development*, *3*(2), 415–444. https://doi.org/10.5194/gmd-3-415-2010
Hogan, R. J., Quaife, T., & Braghiere, R. (2018). Fast matrix treatment of 3-D radiative transfer in vegetation canopies: Spartacus-vegetation 1.1. *Geoscientific Model Development*, *11*(1), 339–350. https://doi.org/10.5194/gmd-11-339-2018
Horn, G. L., Ouwersloot, H. G., Vilà-Guerau de Arellano, J., & Sikma, M. (2015). Cloud shading effects on characteristic boundary-layer length scales. *Boundary-Layer Meteorology*, *157*(2), 237–263. https://doi.org/10.1007/s10546-015-0054-4
Iacono, M. J., Delamere, J. S., Mlawer, E. J., Shephard, M. W., Clough, S. A., & Collins, W. D. (2008). Radiative forcing by long-lived greenhouse gases: Calculations with the AER radiative transfer models. *Journal of Geophysical Research*, *113*, D13103. https://doi.org/10.1029/2008JD009944
Jacobs, C. M. J., & de Bruin, H. A. R. (1997). Predicting regional transpiration at elevated atmospheric CO_2: Influence of the vegetation interaction. *Journal of Applied Meteorology*, *36*(12), 1663–1675. https://doi.org/10.1175/1520-0450(1997)036<1663:PRTAEA>2.0.CO;2
Jacobs, C. M. J., van den Hurk, B. M. M., & de Bruijn, H. A. R. (1996). Stomatal behaviour and photosynthetic rate of unstressed grapevines in semi-arid conditions. *Agricultural and Forest Meteorology*, *80*(2), 111–134. https://doi.org/10.1016/0168-1923(95)02295-3
Jakub, F. (2016). On the impact of three dimensional radiative transfer on cloud evolution (PhD Thesis). Ludwig-Maximilians-Universität München. Retrieved from http://nbn-resolving.de/urn:nbn:de:bvb:19-197226
Jakub, F., & Mayer, B. (2015). A three-dimensional parallel radiative transfer model for atmospheric heating rates for use in cloud resolving models—The tenstream solver. *Journal of Quantitative Spectroscopy and Radiative Transfer*, *163*, 63–71. https://doi.org/10.1016/j.jqsrt.2015.05.003
Jakub, F., & Mayer, B. (2016). 3-D radiative transfer in large-eddy simulations—Experiences coupling the TenStream solver to the UCLA-LES. *Geoscientific Model Development*, *9*(4), 1413–1422.
Jakub, F., & Mayer, B. (2017). The role of 1-D and 3-D radiative heating in the organization of shallow cumulus convection and the formation of cloud streets. *Atmospheric Chemistry and Physics*, *17*(21), 13,317–13,327.
Jonker, H. J. J., Duynkerke, P. G., & Cuijpers, J. W. M. (1999). Mesoscale fluctuations in scalars generated by boundary layer convection. *Journal of the Atmospheric Sciences*, *56*(5), 801–808. https://doi.org/10.1175/1520-0469(1999)056<0801:MFISGB>2.0.CO;2
Kanniah, K. D., Beringer, J., North, P., & Hutley, L. (2012). Control of atmospheric particles on diffuse radiation and terrestrial plant productivity: A review. *Progress in Physical Geography*, *36*(2), 209–237.
Klinger, C., Mayer, B., Jakub, F., Zinner, T., Park, S.-B., & Gentine, P. (2017). Effects of 3-D thermal radiation on the development of a shallow cumulus cloud field. *Atmospheric Chemistry and Physics*, *17*(8), 5477–5500. https://doi.org/10.5194/acp-17-5477-2017
Kobayashi, H., Baldocchi, D. D., Ryu, Y., Chen, Q., Ma, S., Osuna, J. L., & Ustin, S. L. (2012). Modeling energy and carbon fluxes in a heterogeneous oak woodland: A three-dimensional approach. *Agricultural and Forest Meteorology*, *152*, 83–100. https://doi.org/10.1016/j.agrformet.2011.09.008
Li, T., Heuvelink, E., Dueck, T. A., Janse, J., Gort, G., & Marcelis, L. F. M. (2014). Enhancement of crop photosynthesis by diffuse light: Quantifying the contributing factors. *Annals of Botany*, *114*(1), 145–156.
Liou, K. N. (2002). *An introduction to atmospheric radiation*, *International Geophysics* (Vol. 84). Amsterdam, The Netherlands: Academic Press.
Lohou, F., & Patton, E. G. (2014). Surface energy balance and buoyancy response to shallow cumulus shading. *Journal of the Atmospheric Sciences*, *71*(2), 665–682. https://doi.org/10.1175/JAS-D-13-0145.1
Mayer, B. (2009). Radiative transfer in the cloudy atmosphere. *EPJ Web of Conferences*, *1*, 75–99. https://doi.org/10.1140/epjconf/e2009-00912-1
Min, Q. (2005). Impacts of aerosols and clouds on forest-atmosphere carbon exchange. *Journal of Geophysical Research*, *110*, D06203. https://doi.org/10.1029/2004JD004858
Mlawer, E. J., Taubman, S. J., Brown, P. D., Iacono, M. J., & Clough, S. A. (1997). Radiative transfer for inhomogeneous atmospheres: RRTM, a validated correlated-k model for the longwave. *Journal of Geophysical Research*, *102*(D14), 16,663–16,682. https://doi.org/10.1029/97JD00237
Oreopoulos, L., & Barker, H. W. (1999). Accounting for subgrid-scale cloud variability in a multi-layer 1D solar radiative transfer algorithm. *Quarterly Journal of the Royal Meteorological Society*, *125*(553), 301–330. https://doi.org/10.1002/qj.49712555316
Ouwersloot, H. G., Moene, A. F., Attema, J. J., & Vilà-Guerau de Arellano, J. (2017). Large-eddy simulation comparison of neutral flow over a canopy: Sensitivities to physical and numerical conditions, and similarity to other representations. *Boundary-Layer Meteorology*, *162*(1), 71–89. https://doi.org/10.1007/s10546-016-0182-5
Ouwersloot, H. G., Vilà-Guerau de Arellano, J., van Heerwaarden, C. C., Ganzeveld, L. N., Krol, M. C., & Lelieveld, J. (2011). On the segregation of chemical species in a clear boundary layer over heterogeneous land surfaces. *Atmospheric Chemistry and Physics*, *11*(20), 10,681–10,704. https://doi.org/10.5194/acp-11-10681-2011
Pedruzo-Bagazgoitia, X., Ouwersloot, H. G., Sikma, M., van Heerwaarden, C. C., Jacobs, C. M. J., & Vilà-Guerau de Arellano, J. (2017). Direct and diffuse radiation in the shallow-cumulus vegetation system: Enhanced and decreased evapotranspiration regimes. *Journal of Hydrometeorology*, *18*(6), 1731–1748. https://doi.org/10.1175/JHM-D-16-0279.1
Pino, D., Jonker, H. J. J., Vilà-Guerau de Arellano, J., & Dosio, A. (2006). Role of shear and the inversion strength during sunset turbulence over land: Characteristic length scales. *Boundary-Layer Meteorology*, *121*(3), 537–556. https://doi.org/10.1007/s10546-006-9080-6
Ronda, R. J., de Bruin, H. A. R., & Holtslag, A. A. M. (2001). Representation of the canopy conductance in modeling the surface energy budget for low vegetation. *Journal of Applied Meteorology*, *40*(8), 1431–1444. https://doi.org/10.1175/1520-0450(2001)040<1431:ROTCCI>2.0.CO;2
Schlemmer, L., & Hohenegger, C. (2014). The formation of wider and deeper clouds as a result of cold-pool dynamics. *Journal of the Atmospheric Sciences*, *71*(8), 2842–2858. https://doi.org/10.1175/JAS-D-13-0170.1
Schumann, U., Dörnbrack, A., & Mayer, B. (2002). Cloud-shadow effects on the structure of the convective boundary layer. *Meteorologische Zeitschrift*, *11*(4), 285–294. https://doi.org/10.1127/0941-2948/2002/0011-0285

Segal, M., & Davis, J. (1992). The impact of deep cumulus reflection on the ground-level global irradiance. *Journal of Applied Meteorology*, *31*(2), 217–222. https://doi.org/10.1175/1520-0450(1992)031<0217:TIODCR>2.0.CO;2

Sikma, M., Ouwersloot, H. G., Pedruzo-Bagazgoitia, X., van Heerwaarden, C. C., & Vilà-Guerau de Arellano, J. (2018). Interactions between vegetation, atmospheric turbulence and clouds under a wide range of background wind conditions. *Agricultural and Forest Meteorology*, *255*, 31–43. https://doi.org/10.1016/j.agrformet.2017.07.001

Sikma, M., & Vilà-Guerau de Arellano, J. (2019). Substantial reductions in cloud cover and moisture transport by dynamic plant responses. *Geophysical Research Letters*, *46*, 1870–1878. https://doi.org/10.1029/2018GL081236

Stephens, G. L. (1978). Radiation profiles in extended water clouds. II: Parameterization schemes. *Journal of the Atmospheric Sciences*, *35*(11), 2123–2132. https://doi.org/10.1175/1520-0469(1978)035<2123:RPIEWC>2.0.CO;2

Sullivan, P. P., & Patton, E. G. (2011). The effect of mesh resolution on convective boundary layer statistics and structures generated by large-eddy simulation. *Journal of the Atmospheric Sciences*, *68*(10), 2395–2415. https://doi.org/10.1175/JAS-D-10-05010.1

van Heerwaarden, C. C., Vilà-Guerau de Arellano, J., Gounou, A., Guichard, F., & Couvreux, F. (2010). Understanding the daily cycle of evapotranspiration: A method to quantify the influence of forcings and feedbacks. *Journal of Hydrometeorology*, *11*(6), 1405–1422. https://doi.org/10.1175/2010JHM1272.1

Várnai, T., & Davies, R. (1999). Effects of cloud heterogeneities on shortwave radiation: Comparison of cloud-top variability and internal heterogeneity. *Journal of the Atmospheric Sciences*, *56*(24), 4206–4224. https://doi.org/10.1175/1520-0469(1999)056 <4206: EOCHOS>2.0.CO;2

Vilà-Guerau de Arellano, J., Ouwersloot, H. G., Baldocchi, D., & Jacobs, C. M. J. (2014). Shallow cumulus rooted in photosynthesis. *Geophysical Research Letters*, *41*, 1796–1802. https://doi.org/10.1002/2014GL059279

Wapler, K. (2007). Der einfluss des dreidimensionalen strahlungstransportes auf wolkenbildung und-entwicklung (PhD Thesis). Ludwig-Maximilians-Universität München. Retrieved from https://edoc.ub.uni-muenchen.de/6894

Wissmeier, U., Buras, R., & Mayer, B. (2013). paNTICA: A fast 3D radiative transfer scheme to calculate surface solar irradiance for NWP and LES models. *Journal of Applied Meteorology and Climatology*, *52*(8), 1698–1715. https://doi.org/10.1175/JAMC-D-12-0227.1

Zuidema, P., & Evans, K. F. (1998). On the validity of the independent pixel approximation for boundary layer clouds observed during ASTEX. *Journal of Geophysical Research*, *103*(D6), 6059–6074. https://doi.org/10.1029/98JD00080